Chemical Science

ROYAL SOCIETY OF CHEMISTRY

EDGE ARTICLE

View Article Online
View Journal

Cite this: DOI: 10.1039/d6sc01804a

All publication charges for this article have been paid for by the Royal Society of Chemistry

Unravelling the intrinsic thermal conduction mechanism through phonon transport pathway engineering of long-range ordered block copolymers

Kuan Zhang, Junliang Zhang, * Jiahao An and Junwei Gu *

Highly thermally conductive polymers are playing essential roles in various electronics-related fields. However, the mechanism underlying thermal conduction remains hitherto elusive. Herein, the intrinsic thermal conduction mechanism of polymers is disclosed by rational molecular structural design and precise synthesis through reversible addition–fragmentation chain transfer (RAFT) polymerization. By precisely controlling the spatial distribution and sequence of the cyanobiphenyl-based liquid crystalline (LCx) monomer and glycidyl methacrylate (GMA, epoxy-containing unit), as well as the length of the flexible segment $(-CH_2-)_x$ in LCx, block copolymers PLCx$_m$-*b*-PGMA$_n$ with multi-level long-range ordered structures were generated. Specifically, hexagonally packed cylinder-like (HEX-like), lamellar-like (LAM-like), and inverted hexagonally packed cylinder-like (inverted HEX-like) microstructures were effectively constructed as the flexible segment of $-CH_2-$ was increased to 11 ($(-CH_2-)_{11}$, LC11). It is noteworthy that increasing the ratio of LC11 was highly beneficial for enhancing thermal conductivity. Moreover, compared with HEX-like and inverted HEX-like morphologies, which exhibited numerous thermal interfaces, the LAM-like morphology was able to construct long-range phonon transport pathways and reduce phonon scattering through the synergistic effect of microphase separation-driven confined assembly with a semicrystalline structure and supramolecular assembly, thereby exhibiting higher thermal conductivity. This study elucidates the thermal transport mechanism at molecular levels by experiments and simulations, highlighting the crucial role of multiscale chain alignment and long-range ordered structures synergistically enhancing phonon propagation in polymers.

Received 3rd March 2026
Accepted 8th May 2026

DOI: 10.1039/d6sc01804a

rsc.li/chemical-science

Introduction

With the development of electronics towards highly integrated design, high power carrying capacity, and miniaturization and portability, the packaging density per unit volume is increasing exponentially. Consequently, the heat accumulation inside devices has become increasingly severe, inevitably affecting their stability, reliability, and lifespan.[1–3] Polymers exhibit excellent designability, multifunctionality, flexibility, and scalability, making them a promising platform for developing advanced thermal management materials.[4,5] However, conventional polymers normally display low intrinsic thermal conductivity (λ) and cannot meet the urgent demand of highly thermally conductive materials for electronic products.[6–8] Although the thermal conduction of polymers is known to be affected by complex factors, such as molecular chain structure, crystallinity, crystal morphology, molecular chain orientation, and interchain interaction patterns,[9–12] the synergistic effect of multiscale molecular chain structures on heat transfer remains to be elucidated yet.[13,14]

Currently, various strategies have been discovered to enhance the intrinsic thermal conductivity of polymers.[15–19] For instance, increasing the crystallinity or constructing long-range ordered structures with physical lengths exceeding phonon–phonon scattering would increase the phonon mean free path and enable directed heat transfer.[20–22] Also, enhancing interchain interactions through hydrogen bonds or supramolecular interactions (electrostatic, π–π stacking, dipole–dipole interactions, *etc.*) to achieve supramolecular assembly of polymer chains can increase phonon group velocity.[23–25] Chen and coauthors[26] realized long-range orderliness and disentanglement of polymer chains through stretching the polyethylene film. The λ of the stretched polyethylene film reached as high as 62 W (m^{-1} K^{-1}), significantly exceeding those of traditional polymers and even surpassing many metals and ceramics. In our previous studies, epoxies with high intrinsic thermal conductivities were developed by regulating the molecular structures of epoxy monomers to introduce an ordered structure

School of Chemistry and Chemical Engineering, Northwestern Polytechnical University, Xi'an, Shaanxi, 710072, P. R. China. E-mail: junliang.zhang@nwpu.edu.cn; gjw@nwpu.edu.cn

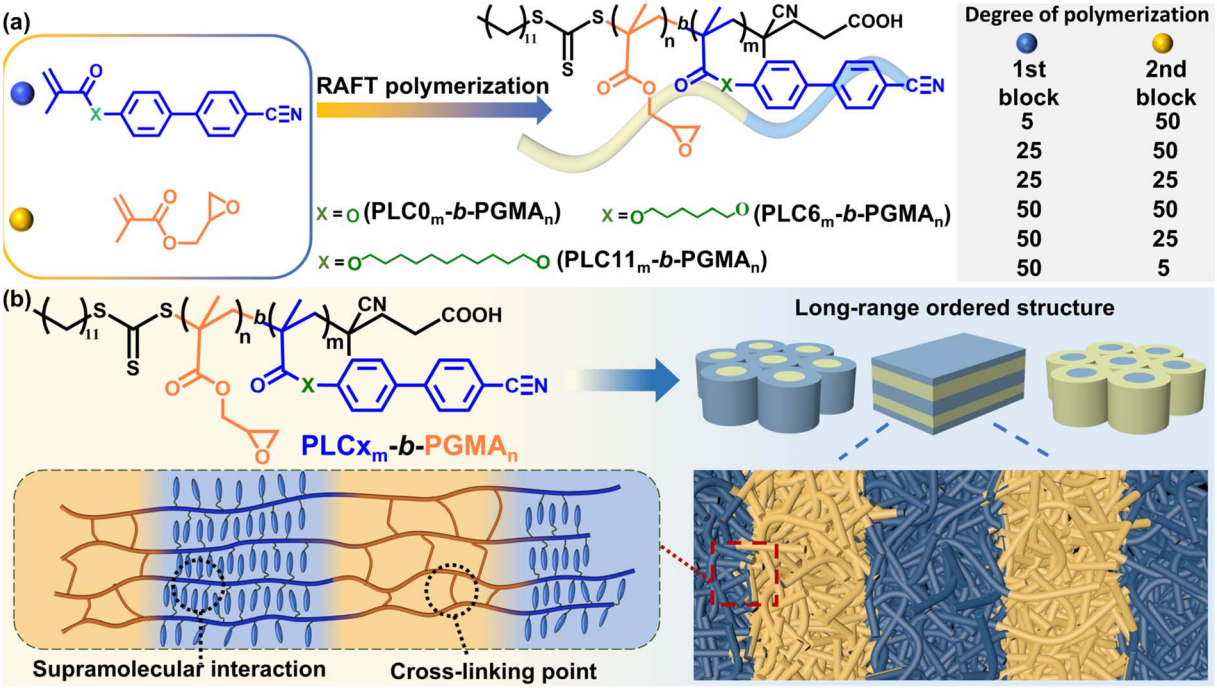

Scheme 1 (a) Schematic diagram for the synthesis of PLCx$_m$-*b*-PGMA$_n$. (b) Schemes for the long-range ordered structures formed by PLCx$_m$-*b*-PGMA$_n$.

into the curing network.[19,21,27,28] However, studies reported to date only indicated that increasing the order degree of polymers or interchain interactions can enhance their intrinsic thermal conductivities.[29–33] Nevertheless, the way of distribution for ordered structures within the polymer network and the relationship between multiscale molecular structures and macroscopic heat transfer properties remain elusive.

The apparent physical properties (including thermal conductivity) of polymers are determined by the orientation and configuration of microstructures at multiple scales (such as atomic, nanoscale, and mesoscopic).[34–36] Controlled polymerization provides an essential platform for exploring the thermal conduction mechanism as polymers with higher-order structures, for instance block or nonlinear copolymers, could be synthesized with defined chemical structures, molecular weight, dispersibility, chain-end characteristics, and multiscale structures on demand.[37–41] Xu *et al.*[42] synthesized a series of block copolymers (BCPs) containing a crystalline block of L-lactide (PLLA) and an azobenzene-based liquid crystalline block through atomic transfer radical polymerization. The formation mechanism of a multi-level long-range ordered structure affected by the interaction of microphase separation, crystallization, and assembly of liquid crystals was investigated. The results indicated that the microphase separation effectively increased the local concentration of liquid crystal units, promoting their orientation and alignment. Additionally, the crystallization behavior of the PLLA segment in BCP enhanced the microphase separation of the block copolymer, further promoting the orientation of liquid crystal units and forming long-range ordered structures. Although polymers with long-range ordered structures have been successfully achieved,[40,43,44] these studies focused only on the construction of long-range ordered structures themselves. The effect of multi-level long-range ordered structures and their dynamic evolution on phonon transmission paths has not been explored yet. In particular, research on the synergistic effect of nanoscale periodic structures formed by microphase separation, supramolecular assembly and polymer crystallization on the thermal conductivity of polymers remains relatively limited. A few studies have preliminarily investigated the influence of microphase-separated morphologies and the degree of phase separation in block copolymers on thermal transport properties.[45,46] However, systematic experimental investigations and in-depth mechanistic understanding of how to synergistically integrate the aforementioned multiple ordered structures to significantly enhance the intrinsic thermal conductivity of polymers are still lacking.

Epoxies, as a typical thermosetting polymer, possess a unique cross-linked structure and a wide range of applications in various fields.[27,28,47] The advancement of high-tech electronic fields has raised tremendous interest in developing intrinsically highly thermally conductive epoxies. However, there is a gap between preparation of intrinsically highly thermally conductive epoxies and their thermal conduction mechanism. This study aims to bridge this gap by providing a universal design principle for preparation of advanced intrinsically highly thermally conductive polymeric materials. Herein, a design strategy is proposed to construct intrinsically highly thermally conductive polymers with multi-level long-range ordered structures through the precise design of polymer molecular structures,

utilizing the synergistic effects of microphase separation, crystallization, and supramolecular assembly. The core of this strategy is to achieve regional restriction of the cyanobiphenyl units through topological structure design of microphase separation, thereby increasing the local concentration of the cyanobiphenyl units. Meanwhile, the semicrystalline properties of polymers were used to regulate the topological structure of the crystalline and amorphous regions, enabling polymer molecular chains to form more orderly supramolecular assembly structures in local regions. Consequently, a phonon transfer network based on a micro-ordered structure was formed to achieve a synergistic improvement in thermal conductivity through the local ordered structure and long-ranged ordered structure (Scheme 1a and b). Specifically, glycidyl methacrylate (GMA) containing an epoxy group and cyanobiphenyl-based liquid crystalline monomers (LCx, $x = 0$, 6, and 11) with varied flexible chain segments $(-CH_2-)_x$ were employed to synthesize block copolymers of PLCx$_m$-*b*-PGMA$_n$ through reversible addition–fragmentation chain transfer (RAFT) polymerization. The synergistic effects of multi-level microstructures on thermal conductivity, as well as the unique role of long-range ordered structures constructed through the synergistic action of microphase separation and supramolecular interactions in thermal conductivity compared to mesoscopic disordered structures, are disclosed for the first time. This work provides an effective approach for the controlled optimization of thermal conductivity in polymeric materials.

Results and discussion

Characterization of LCx and PLCx$_m$-*b*-PGMA$_n$

This study focuses on block copolymers comprising two homopolymer segments of LCx (Scheme S1a) and GMA (Scheme S1b). The composition profiles of these copolymers were designed to be with varying number average degree of polymerization (DP). Specifically, five composition profiles were targeted with reversing the DP of LCx and GMA, which were PLCx$_5$-*b*-PGMA$_{50}$, PLCx$_{25}$-*b*-PGMA$_{50}$, PLCx$_{50}$-*b*-PGMA$_{50}$, PLCx$_{50}$-*b*-PGMA$_{25}$, and PLCx$_{50}$-*b*-PGMA$_5$ (Scheme 1a). Furthermore, to demonstrate the role of molar mass and spatial distribution of monomers, three types of control polymers PLCx$_{25}$-*b*-PGMA$_{25}$, and PLCx$_{50}$-*co*-PGMA$_{50}$ (Scheme S1c), and PLC11$_{50}$ (Scheme S1d) were also synthesized. ^{1}H (Fig. 1a) and ^{13}C (Fig. 1b) nuclear magnetic resonance (NMR) and Fourier transform infrared (FT-IR, Fig. 1c) spectroscopy confirmed the successful synthesis of LCx. The differential scanning calorimetry (DSC, Fig. 1d–f) curves of LC0 demonstrated its crystalline behavior, melting at around 116 °C. As the flexible chain length of LCx increased, LC6 and LC11 exhibited liquid crystalline characters, indicating strong supramolecular assembly abilities. The crystallization enthalpies (ΔH_c) of LC0, LC6, and LC11 were calculated to be 54.48, 54.63, and 81.33 J g^{-1}, respectively. This indicated that the longer flexible side chains of LC11 enhanced molecular mobility and the propensity for ordered packing, thereby promoting crystallization behavior and resulting in the highest ΔH_c.[33,48] However, LC6 only exhibited a melting point at around 64 °C during the heating process while displaying a liquid crystalline cloud point at 37 °C and a crystalline point at 28 °C during the cooling process. This implied that LC6 was a unidirectional liquid crystal, exhibiting liquid crystal phase behavior only during the cooling stage. In contrast, LC11 showed two transition peaks for both the heating and cooling processes. The endothermic peaks at 72 °C and 74 °C in the heating stage were ascribed to the transition from the crystalline phase to the liquid crystalline phase and then to the isotropic liquid phase, respectively. The exothermic peaks of 73 °C and 56 °C corresponded to the transitions of the isotropic liquid phase to the liquid crystalline state and then to the crystalline phase, respectively. It indicated that LC11 was a bidirectional thermotropic liquid crystal capable of achieving liquid crystal phase transitions during both heating and cooling, demonstrating stronger supramolecular assembly abilities than LC6. The polarized optical microscopy (POM) images (Fig. 1g) for LCx exhibited a consistent phenomenon with DSC analyses, showing distinct birefringence at room temperature due to the crystallization behavior. Additionally, the focal-conic fan textures representing the smectic liquid crystalline phase were observed for LC6 and LC11 near the cloud point temperature.

The polymers were first characterized by ^{1}H NMR and ^{13}C NMR spectroscopy (Fig. 1h–i and S1–S4), which confirmed that LCx and GMA were successfully incorporated. Full details of analysis can be found in the SI. Size exclusion chromatography (SEC, Fig. S5–S8 and Tables S1–S3) curves of all the block copolymers displayed a monomodal shape with the second block shifting towards higher molecular weight which matched the theoretical value, indicating successful chain extension *via* RAFT polymerization.[49] The thermal behavior of the polymers was investigated employing DSC. As observed, PLC0$_m$-*b*-PGMA$_n$ (Fig. S9a) showed only one glass transition temperature (T_g) and the T_g increased from 74.3 to 104.5 °C with increasing the ratio of LC0 due to the rigidity of the cyanobiphenyl group, whereas the T_g of PLC6$_m$-*b*-PGMA$_n$ (Fig. S9b) decreased first followed by an increase along with increasing DP of LC6 and finally two T_gs were evident for PLC6$_{50}$-*b*-PGMA$_5$. This is because the flexibility of copolymer side chains significantly increased with increasing the ratio of LC6, resulting in the lower T_g. However, with further increasing LC6 ratio, the higher proportion of cyanobiphenyl group facilitated the formation of ordered stacking through supramolecular assembly. This in turn enhanced segment rigidity and intermolecular interactions, thereby raising the T_g. Simultaneously, microphase separation occurred between the rigid structure and flexible chain segments of the polymer molecules, forming distinct microdomains and thereby generating two independent T_g. In the case of LC11 (Fig. 1j), PLC11$_5$-*b*-PGMA$_{50}$ exhibited only one T_g of 60.7 °C due to the low LC11 content which weakened the phase separation driving force and prevented microphase separation. However, microphase separation was clearly observed while the content of LC11 increased as two T_gs were identified corresponding to the two phases of LC11 and GMA. Meanwhile, these polymers exhibited crystallization behavior as a distinct crystalline melting peak was observed with the crystalline melting enthalpy (ΔH_m, Table S4) of 1.62, 3.01, 5.05, and 8.91 J g^{-1}, respectively. This is primarily

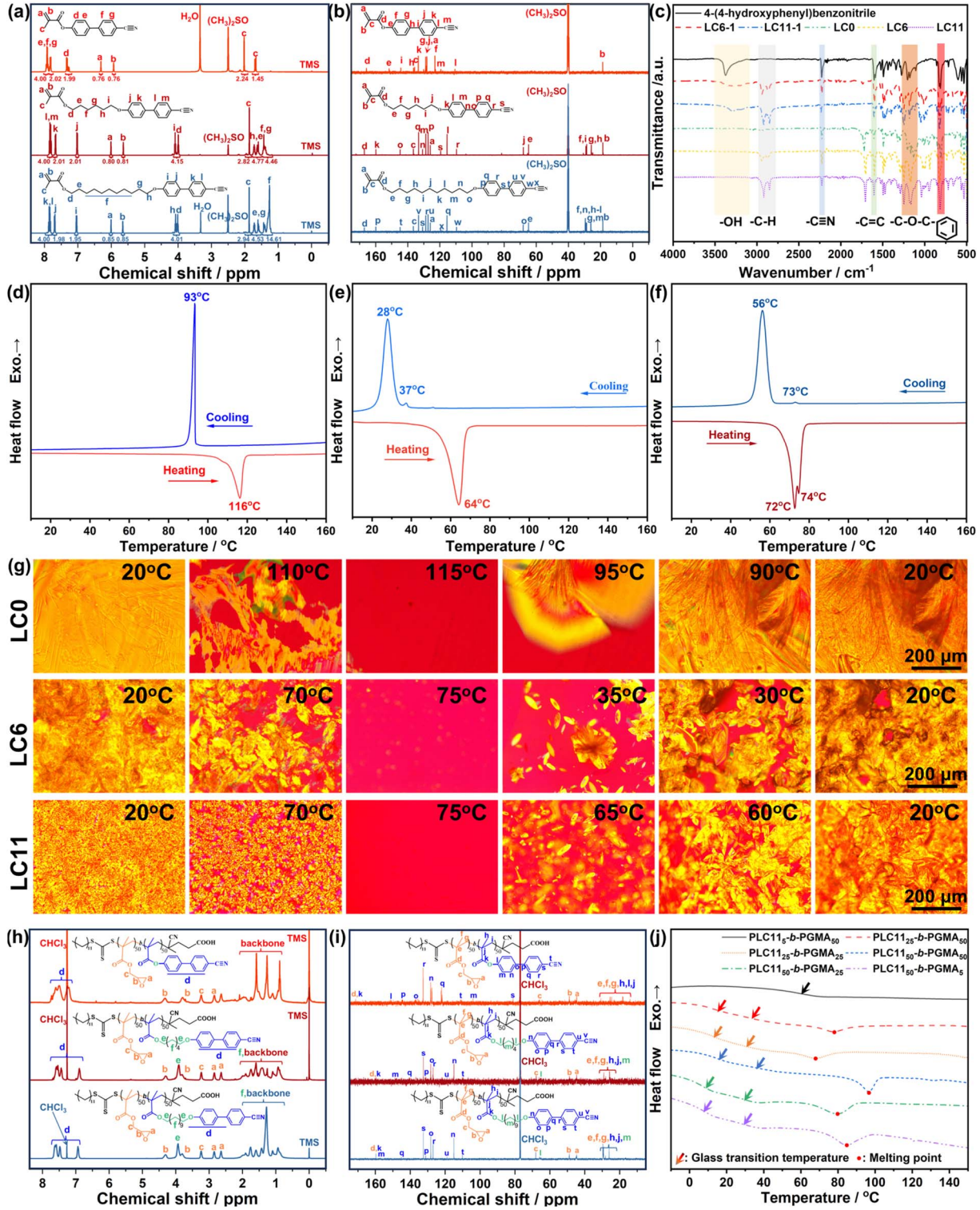

Fig. 1 (a) ^{1}H NMR, (b) ^{13}C NMR, and (c) FT-IR spectra of LCx. DSC curves of (d) LC0, (e) LC6, and (f) LC11. (g) POM images of LCx. (h) ^{1}H NMR and (i) ^{13}C NMR spectra of PLCx$_{50}$-*b*-PGMA$_{50}$. (j) DSC curves of PLC11$_{m}$-*b*-PGMA$_{n}$.

caused by the long flexible chain segment of $(-CH_2-)_{11}$ in LC11, which significantly enhanced the flexibility of the side chains of the copolymer. The improved segmental mobility facilitated the diffusion, alignment, and ordered stacking of polymer chains within the crystal lattice, thereby promoting the crystallization ability.[48,50] Additionally, PLCx$_{50}$-*b*-PGMA$_{50}$ displayed higher T_g and melting point than PLCx$_{25}$-*b*-PGMA$_{25}$ due to the higher molar mass, which was consistent with the Flory–Fox equation

(eqn (S1)). Besides, PLC11$_{50}$-*b*-PGMA$_{50}$ displayed a higher ΔH_m of 3.01 J g^{-1} than its random copolymer counterpart PLC11$_{50}$-*co*-PGMA$_{50}$ (ΔH_m = 2.56 J g^{-1}, Fig. S10). This implied that a more complete crystal structure was resident in the block copolymer PLC11$_{50}$-*b*-PGMA$_{50}$, indicating the stronger crystallization ability than the random copolymer which comprised the same chemical composition.

Microstructure of PLCx$_m$-*b*-PGMA$_n$ and B-ERx$_{m-n}$

The microstructure of PLCx$_m$-*b*-PGMA$_n$ before and after curing was first investigated by wide-angle X-ray diffraction (WAXD). The detailed curing processes can be found in the SI and their thermal characteristic data are summarized in Fig. S11–S15 and Table S5. As displayed in the WAXD curves of PLC0$_m$-*b*-PGMA$_n$ (Fig. S16a), no diffraction peaks were observed at $2\theta < 10°$ due to the large main-chain coupling effect, indicating the failure to form a layered semicrystalline structure.[51] In contrast, strong diffraction peaks at 2θ = 7.10° and 5.15° were evident for PLC6$_m$-*b*-PGMA$_n$ (Fig. S16b) and PLC11$_m$-*b*-PGMA$_n$ (Fig. 2a), respectively. This indicated that the introduction of flexible (–CH$_2$–)$_x$ segments significantly reduced the influence of the main-chain coupling effect, facilitating the formation of a highly ordered semicrystalline structure through supramolecular assembly as well as the multilayer structure. The mechanism of formation of this structure (Fig. 2b) was as follows. The polymer chains folded in a perpendicular direction to the chain axis through supramolecular forces (π–π stacking and dipole–dipole interactions) between cyanobiphenyl units in a long-range order to form crystalline flakes. The polymer chains in each flake were then arranged in parallel and the spacing (d_1 in Fig. 2b, determined by the main diffraction peak of the WAXD curve) between different flakes was maintained

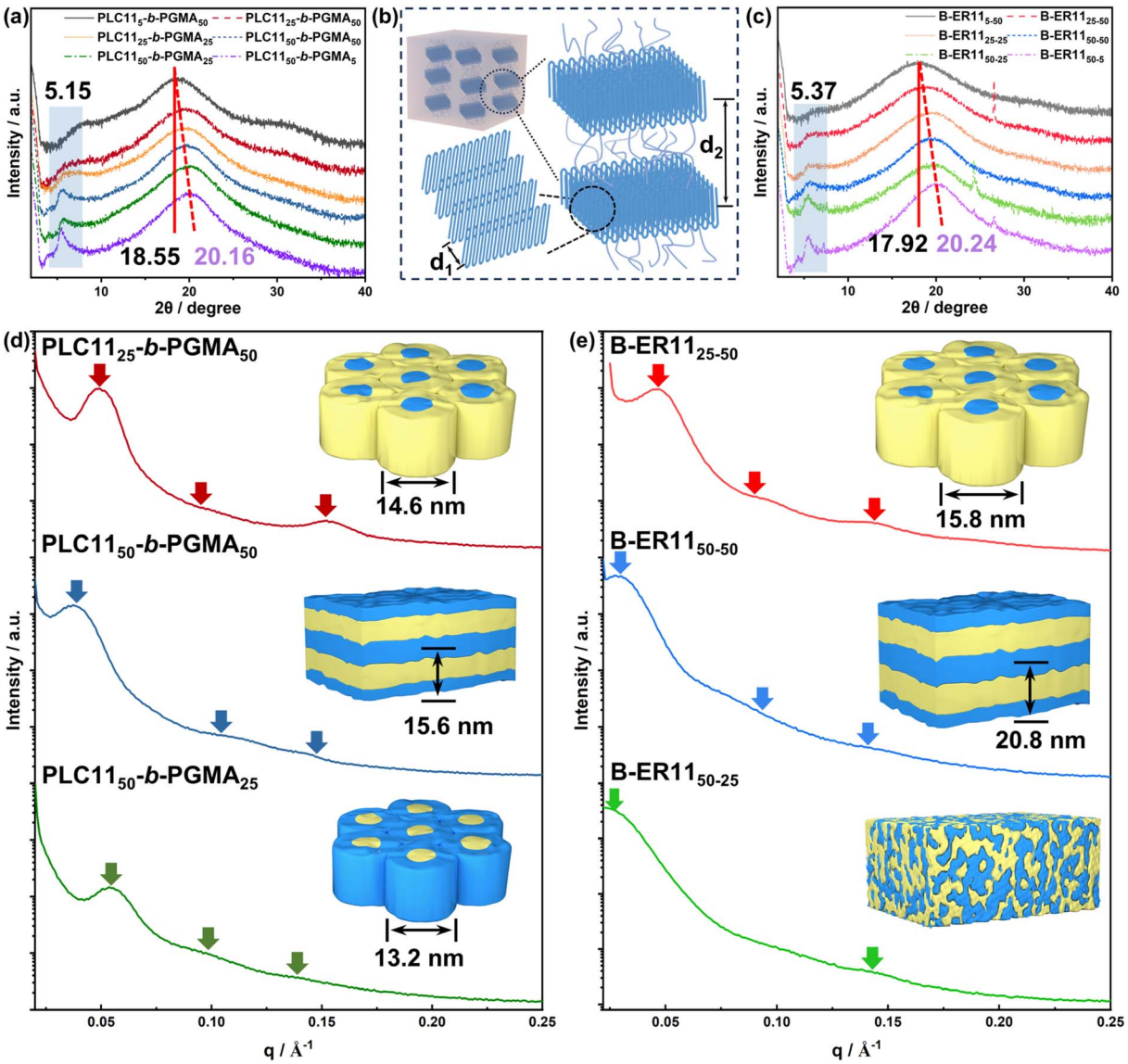

Fig. 2 (a) WAXD curves of PLC11$_m$-*b*-PGMA$_n$. (b) Schematic illustration of the semicrystalline structure and its distribution. (c) WAXD curves of B-ER11$_{m-n}$. Representative SAXS curves of (d) PLC11$_m$-*b*-PGMA$_n$ and (e) B-ER11$_{m-n}$.

relatively uniform. Subsequently, the crystalline flakes assembled into larger lamellar grain structures in amorphous regions, where the grain spacing (d_2 in Fig. 2b, determined by the secondary diffraction peak of the WAXD curve) indicated the way of their distribution.[52]

It is also worth mentioning that the main diffraction peak of PLC0$_m$-*b*-PGMA$_n$ at $2\theta = 18.47°$ (Fig. S16a, $d_1 = 4.80$ Å) and its crystallinity (Fig. S17) remained basically unchanged with increasing ratio of LC0. In contrast, the crystallinity of PLC6$_m$-*b*-PGMA$_n$ and PLC11$_m$-*b*-PGMA$_n$ gradually increased, and the main diffraction peak gradually shifted to higher angles as the ratio of LC6 and LC11 increased, respectively. Specifically, the main diffraction peak of PLC6$_m$-*b*-PGMA$_n$ shifted from $2\theta =$ 18.50° to 19.82° (Fig. S16b), and the crystallinity increased from 8.2% to 14.2%. For PLC11$_m$-*b*-PGMA$_n$, the main diffraction peak shifted from $2\theta = 18.55°$ to 20.16° (Fig. 2a), and the crystallinity increased from 11.0% to 22.3%. According to Bragg equation ($2d \sin\theta = n\lambda$, where λ is the wavelength, Table S6),[53] d_1 decreased from 4.79 Å for PLC6$_5$-*b*-PGMA$_{50}$ to 4.47 Å for PLC6$_{50}$-*b*-PGMA$_5$. Meanwhile, d_1 decreased from 4.77 Å for PLC11$_5$-*b*-PGMA$_{50}$ to 4.40 Å for PLC11$_{50}$-*b*-PGMA$_5$. It is because LC0 lacked flexible chain segments, resulting in a large coupling effect between the cyanobiphenyl unit and the main chain. This hindered the polymer chains from orienting and arranging themselves through supramolecular forces to form crystalline flake structures. Therefore, the order of the supramolecular assembly structure could not be improved even if the ratio of LC0 increased, resulting in no changes in the crystallinity, the main diffraction peak, and d_1 of PLC0$_m$-*b*-PGMA$_n$. However, as the length of the flexible chain segment $(-CH_2-)_x$ in LCx increased, the polymer main chain and side chains were decoupled. Consequently, the influence of supramolecular force increased, causing the crystallization ability to increase, and the crystal zone structure to gradually improve with increasing the ratio of LC6 and LC11. Thus, the main diffraction peak gradually shifted to higher angles, showing a gradually decreased d_1. This was further verified by the fact that the homopolymer PLC11$_{50}$ exhibited the smallest d_1 (4.38 Å, Fig. S18a). Due to the greatest flexibility, PLC11$_m$-*b*-PGMA$_n$ exhibited the largest increase in crystallinity and the largest shift of the main diffraction peak (the smallest d_1), which suggested the presence of the highest order of supramolecular assembly and the largest crystal stacking density. Meanwhile, the d_2 of PLC6$_m$-*b*-PGMA$_n$ and PLC11$_m$-*b*-PGMA$_n$ (except PLC6$_5$-*b*-PGMA$_{50}$ and PLC11$_5$-*b*-PGMA$_{50}$) were 12.44 and 17.14 Å, respectively. This is because as the flexible segment length of LCx increased, both the volume of the side chain and amorphous region increased, causing the thickness (d_2) of the lamellar crystal grain structure layer to increase. It is worth noting that the diffraction peak at $2\theta = 5.15°$ of PLC11$_{50}$-*b*-PGMA$_{50}$ (Fig. 2a) was much sharper than that of PLC11$_{50}$-*co*-PGMA$_{50}$ (Fig. S18b), suggesting its more ordered semicrystalline structure than that of the random copolymer with the same chemical composition.

The WAXD curves of PLCx$_m$-*b*-PGMA$_n$ after curing (B-ERx$_{m-n}$) are illustrated in Fig. 2c and S19. Based on the results calculated using the Bragg equation (Table S7), d_1 of B-ERx$_{m-n}$ decreased as the ratio of LCx increased for the same block copolymer while it showed the same decreasing trend for the polymers with the same monomer ratio as the flexible segment length of LCx increased. Among these, B-ER11$_{50-5}$ exhibited the smallest d_1 of 4.38 Å (Fig. 2c). This is because π–π stacking and dipole–dipole interactions between polymer chains would be enhanced as the ratio of LCx increased which strengthened the intermolecular forces. Besides, the increased flexible side chain length would lead to a higher degree of rotational freedom within polymer chains, which was greatly affected by the supramolecular forces. The synergistic effect of these two factors led to the formation of the densest and most orderly lamellar grain structure of B-ER11$_{50-5}$. Meanwhile, for B-ER0$_{m-n}$, when the monomer ratio of LC0/GMA > 25/50, it exhibited a lamellar semicrystalline structure with $d_2 = 21.53$ Å (Fig. S19a and Table S7). And its d_2 value was larger than the 12.23 Å of B-ER6$_{50-25}$ and B-ER6$_{50-5}$ in B-ER6$_{m-n}$ and 16.44 Å of B-ER11$_{m-n}$. This is because there were no flexible chain segments between the main chain and side chains of B-ER0$_{m-n}$, which resulted in a large cooperative interaction between the main and side chains. Therefore, the semicrystalline lamellar grains formed were structurally interfered by the main chain, leading to an increase in the grain spacing, whereas, due to the small coupling effect between the main and side chains of B-ER6$_{m-n}$ and B-ER11$_{m-n}$, the main and side chains have sufficient freedom to arrange themselves in an orderly manner, thus forming a more regular and orderly semicrystalline structure and a smaller d_2. Additionally, the volume of the amorphous region in B-ER6$_{m-n}$ and B-ER11$_{m-n}$ was proportional to the side chain volume, resulting in the larger d_2 for B-ER11$_{m-n}$ than B-ER6$_{m-n}$. It should be noted that the diffraction peak observed at $2\theta = 4.10°$ for B-ER0$_{m-n}$ (Fig. S19a) was attributed to the decoupling role during the curing process, which reduced the influence of the main chain on the supramolecular assembly and crystallization behavior, resulting in the formation of a semicrystalline structure. Furthermore, the crystallinity of B-ER11$_{m-n}$ increased with both the length of the flexible chain segment $(-CH_2-)_x$ and the ratio of LCx (Fig. S20), with B-ER11$_{50-5}$ exhibiting the highest crystallinity of 21.1%. This is because the high LCx ratio promoted the formation of crystalline regions while the flexible chain segments facilitated the ordered arrangement of molecular chains into the crystal lattice.

SAXS was further employed to investigate the microstructures of PLCx$_m$-*b*-PGMA$_n$ and B-ERx$_{m-n}$. As exhibited in Fig. S21, the degree of microphase separation was enhanced with increasing the length of the flexible chain segment $(-CH_2-)_x$ in LCx. PLC0$_m$-*b*-PGMA$_n$ showed no scattering peaks (Fig. S21a), indicating a uniform electron density and a homogeneous aggregated state structure. PLC6$_m$-*b*-PGMA$_n$ exhibited first-order scattering peaks only in certain polymers and did not show any clear higher-order scattering peaks (Fig. S21b), indicative of imperfect microphase separation structures with poor order and defects.[54] By contrast, PLC11$_{25}$-*b*-PGMA$_{50}$, PLC11$_{25}$-*b*-PGMA$_{25}$, PLC11$_{50}$-*b*-PGMA$_{50}$, and PLC11$_{50}$-*b*-PGMA$_{25}$ exhibited broadened first-order and higher-order scattering peaks, suggesting the formation of microphase separation structures with a certain degree of order (Fig. S21c). Among these, three

scattering peaks can be observed for PLC11$_{25}$-*b*-PGMA$_{50}$ with scattering vector ratio ($q_1 : q_2 : q_3$) approximately equal to $1 : \sqrt{3} : 3$ (Fig. 2d), indicative of a hexagonally packed cylinder-like (HEX-like) morphology, with the lattice parameter (a, calculated using the Bragg equation according to the reflection of the first-order scattering peak of the SAXS curve,[55,56] Table S8) of 14.6 nm. Meanwhile, PLC11$_{25}$-*b*-PGMA$_{25}$ (Fig. S21c) and PLC11$_{50}$-*b*-PGMA$_{50}$ also showed three broadened reflections with $q_1 : q_2 : q_3$ approximately equal to $1 : 2 : 3$ and $1 : 3 : 4$, respectively, indicating the presence of lamellar-like (LAM-like) morphology, with a being 10.7 and 15.6 nm, respectively. Furthermore, PLC11$_{50}$-*b*-PGMA$_{25}$ demonstrated three scattering peaks with $q_1 : q_2 : q_3$ approximately equal to $1 : \sqrt{3} : \sqrt{7}$, indicating the presence of inverted hexagonally packed cylinder-like (inverted HEX-like) morphology with $a = 13.2$ nm. The homopolymer PLC11$_{50}$ exhibited only one diffuse scattering peak at $q = 0.146$ Å^{-1} (Fig. S22a), indicating no periodic morphology and no microphase separation. Similarly, the random copolymer PLC11$_{50}$-*co*-PGMA$_{50}$ exhibited only one main broad scattering peak at $q = 0.116$ Å^{-1} (Fig. S22b), indicating the absence of long-range order although it had the same chemical composition with PLC11$_{50}$-*b*-PGMA$_{50}$. This is attributed to the random monomer distribution characteristics of PLC11$_{50}$-*co*-PGMA$_{50}$ which restricted the formation of ordered periodic morphology.

The SAXS curves of cured polymers B-ERx$_{m-n}$ are shown in Fig. 2e and S23. As can be seen, the microphase separation of PLCx$_m$-*b*-PGMA$_n$ was retained to a certain degree after curing, especially for PLC11$_m$-*b*-PGMA$_n$ (Fig. 2e). For instance, three broadened reflexes were observed for B-ER11$_{25-50}$ with $q_1 : q_2 : q_3$ approximately equal to $1 : \sqrt{3} : 3$, indicating a HEX-like morphology with $a = 15.8$ nm. Meanwhile, B-ER11$_{50-50}$ exhibited three scattering peaks with $q_1 : q_2 : q_3$ approximately equal to $1 : 3 : 4$, implying a LAM-like morphology with $a = 20.8$ nm. However, B-ER11$_{50-25}$ exhibited only a primary diffraction peak and high order peaks (Fig. S24), indicating that the inverted HEX-like structure formed by PLC11$_{50}$-*b*-PGMA$_{25}$ was distorted during the curing process, resulting in a decrease of long-range order. Meanwhile, it should be noted that B-ER11$_{25-25}$ (Fig. S23c) showed no reflections indicating that the LAM-like morphology disappeared completely after curing. This is, however, in contrast to B-ER11$_{50-50}$ where the LAM-like morphology was retained. It is because the lattice parameter ($a = 15.6$ nm) of PLC11$_{50}$-*b*-PGMA$_{50}$ was larger than that of PLC11$_{25}$-*b*-PGMA$_{25}$ ($a = 10.7$ nm), suggesting that the layer of LAM-like morphology formed by PLC11$_{50}$-*b*-PGMA$_{50}$ was thicker which was difficult to destruct by the curing reaction. In addition, R-ER11$_{50-50}$ cured from the random copolymer PLC11$_{50}$-*co*-PGMA$_{50}$ exhibited no reflexes (Fig. S25), indicating the absence of microphase separation. This is attributed to its random monomer distribution, which prevented the formation of a long-range ordered structure. Notably, based on the SAXS fitting results (Table S8), the microphase separated structure formed by PLC11$_m$-*b*-PGMA$_n$ and B-ER11$_{m-n}$ exhibited a certain degree of distortion.[57] This may be because the interaction parameter between the monomers of the block copolymer was relatively low, resulting in insufficient driving force for phase separation. Moreover, the destructive interference between the microphase separated structure and the lamellar crystalline structure of the semicrystalline polymer led to the absence of low-order diffraction peaks in some samples.[55] Additionally, considering that no alignment treatment was applied to the samples, it would be reasonable for the samples to form imperfect lamellar or hexagonally packed cylinder morphologies.

Thermal conductivities of PLCx$_m$-*b*-PGMA$_n$ and B-ERx$_{m-n}$

The intrinsic λ values of PLCx$_m$-*b*-PGMA$_n$ were first measured. As shown in Fig. 3a and Table S6, the λ of PLCx$_m$-*b*-PGMA$_n$ increased with the increase of flexible chain segment $(-CH_2-)_x$ length under the same LCx ratio. For the same LCx, λ generally increased with increasing the LCx ratio. Among these, PLC11$_{50}$-*b*-PGMA$_5$ exhibited the highest λ of 0.29 W (m^{-1} K^{-1}). This is because LCx containing long flexible chain segments could form a dense and ordered lamellar morphology through π–π stacking and dipole–dipole interactions of the cyanobiphenyl units (see the comparative analysis in Fig. 2a and S16). Consequently, the phonon scattering would be reduced due to the thermal vibrations of the orderly arranged crystal lattices in the crystalline regions. The phonon mean free path would thus be increased which effectively enhanced the intrinsic thermal conductivity of PLCx$_m$-*b*-PGMA$_n$. Additionally, due to the more regular and ordered semicrystalline structure (see the analysis in Fig. 2a), PLC11$_m$-*b*-PGMA$_n$ exhibited higher λ than PLC6$_m$-*b*-PGMA$_n$. Besides, the interflake spacing of the supramolecular assembled structure decreased with increasing the ratio of LCx which increased the packing density of crystalline flakes within the lamellar crystallites. Therefore, phonon scattering would be suppressed, resulting in the enhanced λ. Furthermore, the theory that supramolecular interactions of cyanobiphenyl units drive self-assembly to achieve enhanced thermal conductivity was verified by the homopolymer PLC11$_{50}$. The results showed that, due to its 100% content of cyanobiphenyl units, PLC11$_{50}$ achieved a higher thermal conductivity of 0.33 W (m^{-1} K^{-1}) (Table S6) compared to PLC11$_{50}$-*b*-PGMA$_5$, without relying on a LAM-like morphology for regional dense packing of the cyanobiphenyl units. Notably, PLC11$_{50}$-*b*-PGMA$_{50}$ exhibited a higher λ although it contained a lower LCx ratio compared to PLC11$_{50}$-*b*-PGMA$_{25}$. This is because the multi-level long-range ordered LAM-like morphology in PLC11$_{50}$-*b*-PGMA$_{50}$ effectively increased the local concentration of cyanobiphenyl units, which enhanced the microscopic structural order and reduced defects within the polymer. Consequently, the thermal conduction ability was improved due to the optimized local ordered structure and thermal conduction pathways, which suppressed phonon scattering and increased the phonon mean free path.

It is notable that block copolymers PLCx$_{50}$-*b*-PGMA$_{50}$ and random copolymers PLCx$_{50}$-*co*-PGMA$_{50}$ exhibited basically unchanged λ when $x = 0$ and 6 (Fig. 3b). In the case of x being 11, the λ of the random copolymer PLC11$_{50}$-*co*-PGMA$_{50}$ was 0.22 W (m^{-1} K^{-1}), whereas that of the block copolymer PLC11$_{50}$-*b*-PGMA$_{50}$ increased to 0.27 W (m^{-1} K^{-1}), representing a 23% improvement. This is because both PLC6$_{50}$-*b*-PGMA$_{50}$ and PLC6$_{50}$-*co*-PGMA$_{50}$ lacked multi-level long-range order.

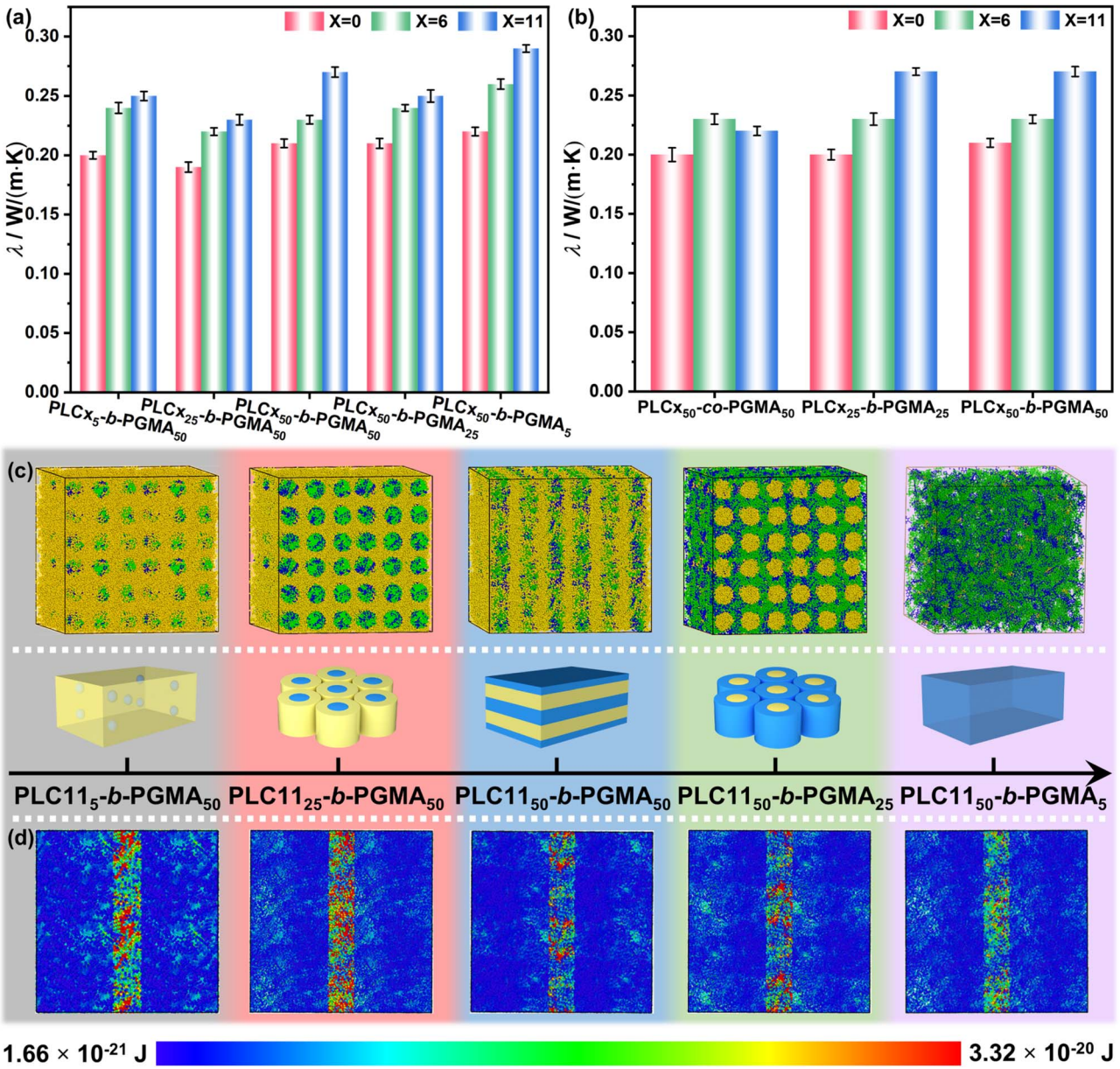

Fig. 3 The experimental λ values of (a) PLCx$_m$-*b*-PGMA$_n$ and (b) comparison with control polymers. (c) Schemes of microstructure and (d) kinetic energy of atom in the NEMD process of different block copolymers PLC11$_m$-*b*-PGMA$_n$.

Therefore, their intrinsic λ was mainly related to the ratio of cyanobiphenyl units, thus leading to the similar λ. In contrast, LAM-like multi-level ordered morphology was formed within PLC11$_{50}$-*b*-PGMA$_{50}$ but not within PLC11$_{50}$-*co*-PGMA$_{50}$. Therefore, the λ was enhanced for PLC11$_{50}$-*b*-PGMA$_{50}$. Most notably, block copolymers PLCx$_{25}$-*b*-PGMA$_{25}$ and PLCx$_{50}$-*b*-PGMA$_{50}$ with the same LCx showed nearly identical λ. This indicated that the molar mass of the polymers did not affect their intrinsic thermal conductivity when the ratios of LCx and the microphase morphology were the same.

Next, molecular dynamics simulation was applied to block copolymers PLC11$_m$-*b*-PGMA$_n$ to investigate the effects of monomer ratio, supramolecular assembly, and semicrystalline structures on the multi-level long-range order.[58,59] Furthermore, thermal conduction was simulated in different multi-level long-range ordered structures to analyze the influence of the microstructure on thermal conductivity. First, the molecular dynamics model of the microphase morphology of PLC11$_m$-*b*-PGMA$_n$ was established using Packmol. Specifically, 255 polymer chains were placed in a box of 100 × 100 × 100 Å and the monomer units for LC11 and GMA in each polymer chain were *m* and *n*, respectively. The cyanobiphenyl group was simulated using the optimized potentials for liquid simulations (OPLS) force field. Atoms in different structures were distinguished by different colors where yellow represented epoxy groups, green denoted flexible chain segments (–CH$_2$–)$_x$, and blue indicated cyanobiphenyl units.

As shown in Fig. 3c, the microphase structure was found to evolve from spherical (SPH) to HEX, layered (LAM), and inverted HEX morphology, respectively, when the monomer ratio of LC11 to GMA was varied from 5–50 to 50–25, followed by the disappearance of microphase separation for 50–5. The simulation results agreed with SAXS analysis (Fig. 2d), further demonstrating that multi-level long-range ordered structures could be effectively constructed through microphase separation and supramolecular assembly of block copolymers. Next, the constructed model of the multi-level long-range ordered structure was exported as a Lammps-readable force field data file,[60] and thermal conductivity was calculated using non equilibrium molecular dynamics (NEMD) simulations. Then, the geometry was optimized *via* relaxation in a microcanonical ensemble at room temperature.[61] A heat source was set at the center of the material to inject heat, and cold sources were set at both ends to extract heat. The kinetic energy of each atom was colored, with redder colors indicating higher kinetic energy, as shown in Fig. 3d. Due to differences in thermal conduction rates of the long-range ordered structures of PLC11$_m$-*b*-PGMA$_n$, the atomic kinetic energy of these polymers exhibited significant variation. Here, PLC11$_{50}$-*b*-PGMA$_5$ exhibited the most uniform kinetic energy distribution, with gentle color gradation indicating that it had a low temperature gradient, rapid heat diffusion, and the highest heat transport speed. During the simulation, the energy flux (dQ) and temperature gradient (dT/dZ) within the material were calculated. After simulation, the thermal conductivity of the material was calculated in the non-equilibrium state using eqn (1):

$$\lambda = -\mathrm{d}Q \times \frac{\mathrm{d}Z}{\mathrm{d}T} \quad (1)$$

The temperature gradient distribution during simulation is shown in Fig. 4a. It was observed that the temperature gradient distribution was correlated with the linear response condition, indicating that the thermal conductivity calculated using the NEMD method was stable and reliable. As shown in Fig. 4b, PLC11$_{50}$-*b*-PGMA$_5$ exhibited the highest simulated λ of 1.25 W (m^{-1} K^{-1}). This is because PLC11$_{50}$-*b*-PGMA$_5$ contained the highest concentration of cyanobiphenyl units. Through the dipole–dipole and π–π stacking interactions of the cyanobiphenyl units, a highly uniform and ordered supramolecular assembled structure was formed within the polymer, which resulted in the fewest thermal interfaces and the lowest interfacial thermal resistance, thereby the highest λ. Here it is worth mentioning that PLC11$_{50}$-*b*-PGMA$_{50}$ exhibited a higher simulated λ of 1.12 W (m^{-1} K^{-1}) although it contained a lower ratio of LCx compared to PLC11$_{50}$-*b*-PGMA$_{25}$, the simulated λ of which was 1.05 W (m^{-1} K^{-1}). As aforementioned, the enhanced λ of PLC11$_{50}$-*b*-PGMA$_{50}$ was achieved through multiple structural synergistic effects, the thermal conduction mechanism of which is illustrated in Fig. 4c. First, a lamellar morphology was formed through microphase separation within PLC11$_{50}$-*b*-PGMA$_{50}$, which significantly increased the concentration of cyanobiphenyl units in localized regions, thereby enhancing the ability of supramolecular interactions and promoting the formation of highly ordered supramolecular assembled structures. Meanwhile, the semicrystalline structure of the polymer played a crucial role in the following two aspects. On one hand, the interfacial tension between crystalline and amorphous domains enhanced the microphase separation of the polymer, improving the topological order of the polymer microphase separation structure. On the other hand, the crystalline network provided rigid support for the supramolecular assembly system formed by cyanobiphenyl units, which significantly enhanced its structural stability. This synergistic construction mechanism based on microphase separation, crystallization regulation, and supramolecular assembly ultimately formed the LAM multi-level long-range ordered structure. Therefore, an optimized continuous phonon transport network at the mesoscopic scale was achieved through ordered molecular-scale arrangement, thereby increasing the phonon mean free path and effectively enhancing the intrinsic thermal conductivity of PLC11$_{50}$-*b*-PGMA$_{50}$. By contrast, the multi-level long-range ordered structures of SPH, HEX, and inverted HEX formed by PLC11$_5$-*b*-PGMA$_{50}$, PLC11$_{25}$-*b*-PGMA$_{50}$, and PLC11$_{50}$-*b*-PGMA$_{25}$, respectively, exhibited discontinuous heat conduction pathways and numerous thermal interfaces, leading to severe phonon scattering and lower thermal conductivity. Notably, the simulation λ exhibited the same trend but higher values than the experimental λ. This is because the molecular dynamics simulation employed an idealized standard model, which generated ideally highly ordered multi-level long-range ordered structures that did not consider any defects in the actual preparation process. The consistent trends between simulation and experimental results further validated that the intrinsic thermal conductivity of polymers could be enhanced through phonon transport pathway engineering by optimizing the long-range ordered structure.

Fig. 5a and Table S7 show the experimental λ for B-ERx$_{m-n}$. As can be seen, the λ of B-ERx$_{m-n}$ increased with increasing the length of (–CH$_2$–)$_x$ in LCx for the same monomer ratio. Furthermore, the λ of B-ERx$_{m-n}$ with the same LCx generally increased with increasing the ratio of LCx. Among these, B-ER11$_{50-5}$ exhibited the highest intrinsic thermal conductivity, with its λ improving to 0.39 W (m^{-1} K^{-1}) from 0.32 W (m^{-1} K^{-1}) of B-ER11$_{5-50}$, which was 1.95 times that of conventional epoxy resin (E-51, 0.20 W (m^{-1} K^{-1})).[28] This is because, with increasing the flexible chain segment length and the monomer ratio of LCx, the intermolecular supramolecular forces become strengthened. This resulted in a reduction of the interflake distances within the lamellar crystallites, thus forming a compact supramolecular assembled structure and a semicrystalline structure. The phonon scattering would be suppressed and the thermal conductivity would therefore be enhanced. It is however noteworthy that although B-ER11$_{50-50}$ contained a lower monomer ratio of LC11, it exhibited a higher λ of 0.37 W (m^{-1} K^{-1}) than 0.35 W (m^{-1} K^{-1}) of B-ER11$_{50-25}$. This is mainly ascribed to its retained LAM-like multi-level long-range ordered structure (see the analysis in Fig. 2e), which still provided a synergistic enhancement on the thermal conductivity within the crosslinked structure. It is also worth mentioning that B-ER11$_{50-50}$ displayed a 28% higher λ than 0.29

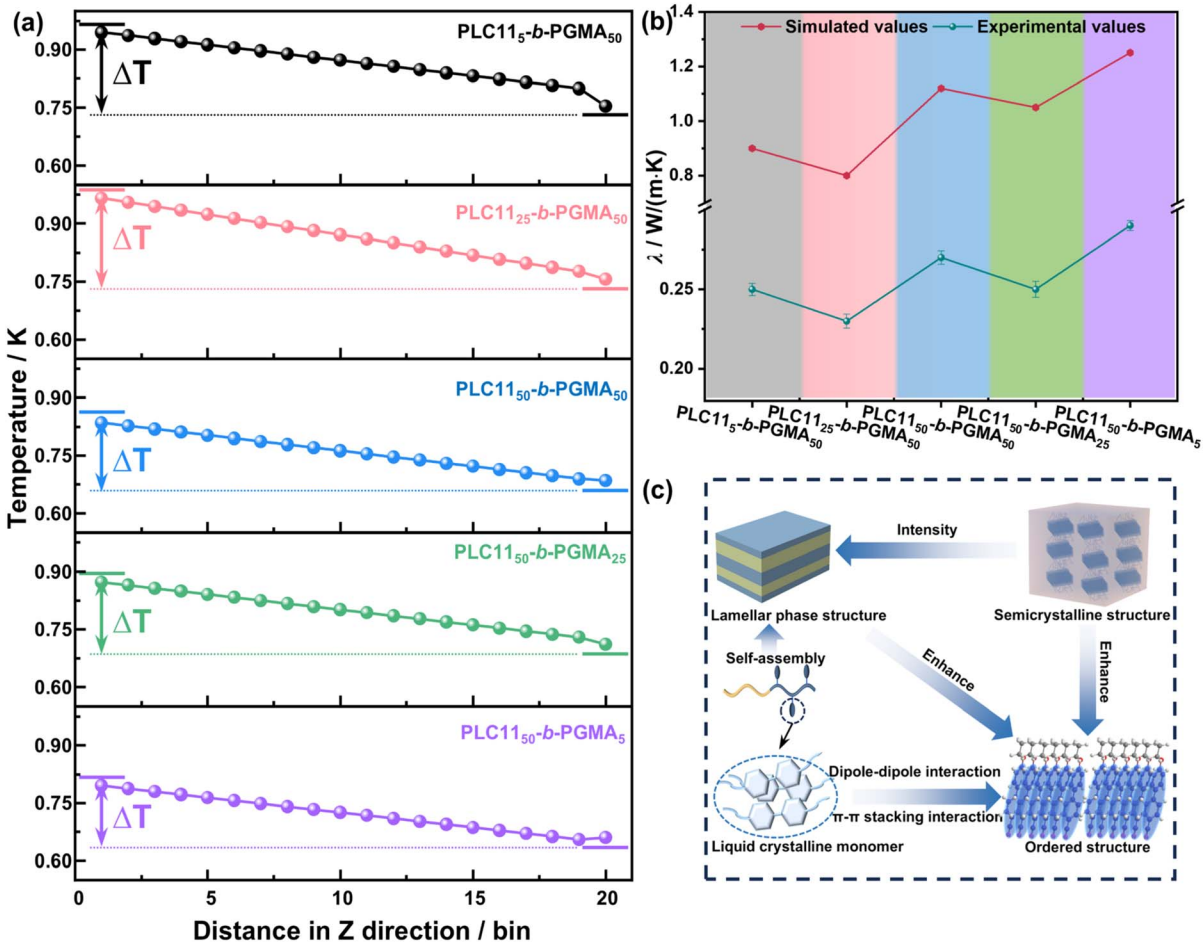

Fig. 4 (a) Temperature gradient distribution, (b) simulated and experimental λ values of PLC11$_m$-*b*-PGMA$_n$. (c) Thermal conduction mechanism of LAM-type multi-level long-range ordered structures.

W (m^{-1} K^{-1}) of R-ER11$_{50-50}$ (Fig. S26) even though their polymer precursors had the same chemical composition. Notably, B-ER11$_{25-25}$ demonstrated a lower λ of 0.30 W (m^{-1} K^{-1}) than B-ER11$_{50-50}$ although their uncured polymer precursors exhibited nearly identical λ. This is mainly attributed to the disruption of the multi-level long-range ordered structure of PLC11$_{25}$-*b*-PGMA$_{25}$ after curing, which increased the disorder of the cured network. These results further confirmed that the multi-level long-range ordered structure of LAM-like morphology could effectively enhance the intrinsic thermal conductivity of polymers. It is worth noting that B-ER0$_{m-n}$, B-ER6$_{m-n}$ and B-ER11$_{m-n}$ exhibited higher λ than their polymer precursors, indicating that the cured densely cross-linked network effectively enhanced their intrinsic thermal conductivity. Furthermore, it indicated that the microscopic structural order of the cross-linked network was significantly affected by the flexible chain segment (–CH$_2$–)$_x$ length of LCx. This is because the densely cross-linked network after curing reduced internal defects within the material, increased the phonon mean free path, suppressed phonon scattering, and enhanced the λ. However, in the case of LC0, there was a significant cooperative interaction between the main and side chains, which interfered with the formation of an ordered structure, resulting in the very slight improvement of λ.

The thermal infrared images of B-ER11$_{m-n}$ (Fig. 5b) and the corresponding time-dependent temperature profiles (Fig. S27) displayed a consistent trend with the measured λ. B-ER11$_{50-5}$ exhibited the fastest heating rate, reaching the highest 74.6 °C after 120 seconds. Additionally, finite element simulation (FES) analysis was conducted to evaluate the heat dissipation capability of B-ER11$_{m-n}$ in semiconductor chip packaging. Fig. 5c shows a schematic diagram of the FES model for a semiconductor chip in a plastic ball grid array (PBGA) package. The FES simulation results for a semiconductor chip packaged with B-ER11$_{m-n}$ are displayed in Fig. 5d. It can be observed that when traditional epoxy resin (E-51) was applied as the packaging material, the surface temperature of the high-power silicon chip reached the highest of 169.5 °C. By contrast, when B-ER11$_{m-n}$ was employed as the packaging material, the maximum surface temperature of the corresponding high-power silicon chip declined significantly, which was consistent with the λ values. The maximum surface temperature of the high-power silicon chips packaged with B-ER11$_{50-5}$ only reached 147.4 °C, decreased by 22.1 °C compared to that of traditional epoxy resin packaging. This is primarily ascribed to the high thermal

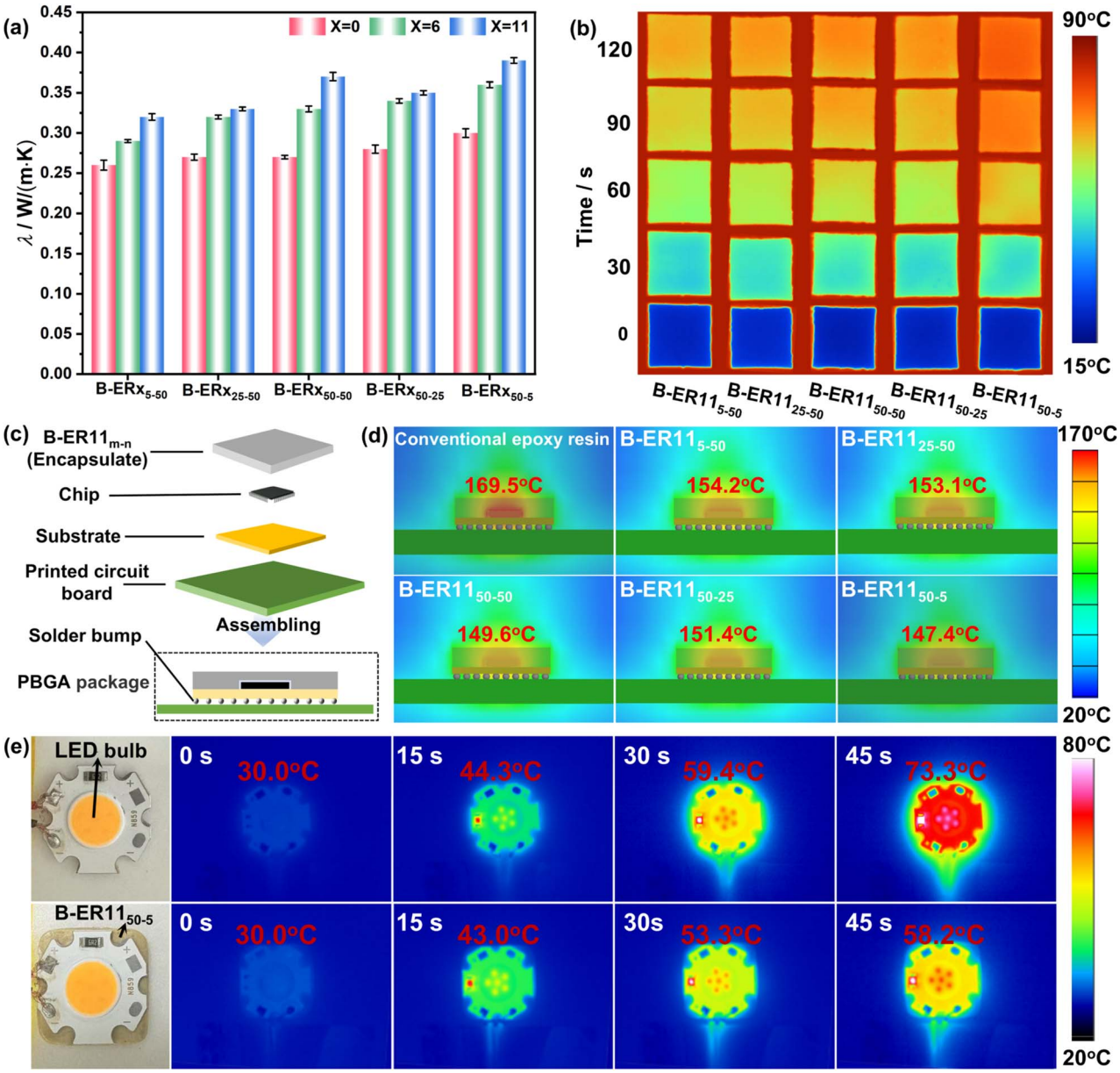

Fig. 5 (a) The experimental λ values of B-ERx$_{m-n}$. (b) Infrared thermal imaging photos of B-ER11$_{m-n}$. (c) Schematic diagram of the FES model for a plastic ball grid array package. (d) FES simulation results. (e) Experimental setup with infrared recordings for LED bulb thermal management applying B-ER11$_{50-5}$ as TIMs.

conductivity of B-ER11$_{m-n}$, which enabled it to quickly transfer and dissipate the large amount of heat generated by the chip into the surrounding environment. The FES results demonstrated that B-ER11$_{m-n}$, especially B-ER11$_{50-5}$, exhibited excellent heat dissipation capabilities and efficient thermal management performance when used as a packaging material, capable of meeting the thermal management requirements of 5G electronic devices in practical applications. The application of B-ER11$_{50-5}$ as a thermal interface material (TIM) was investigated using an LED bulb (Fig. 5e). As clearly observed, the operating temperature of the LED bulb reached 73.3 °C after 45 seconds when no thermal interface material was applied. Notably, the temperature of the LED bulb was only 58.2 °C when B-ER11$_{50-5}$ was used as the TIM, showing a significant reduction of 15.1 °C. The above results indicated that B-ER11$_{50-5}$ could be applied as an efficient TIM due to its high intrinsic thermal conductivity.

Conclusions

In this work, a series of sequence-controlled block copolymers PLCx$_m$-*b*-PGMA$_n$ based on cyanobiphenyl and epoxy units with varied monomer ratios were synthesized by RAFT polymerization. The results revealed that by precisely controlling the spatial distribution and sequence of LCx and GMA, as well as the length of flexible segments (–CH$_2$–)$_x$ in LCx, multi-level long-

range ordered structures of hexagonally packed cylinder-like (HEX-like), lamellar-like (LAM-like), and inverted hexagonally packed cylinder-like (inverted HEX-like) morphologies within the polymer (PLC11$_m$-*b*-PGMA$_n$) were generated effectively. It is noteworthy that increasing the ratio of LC11 was highly beneficial for enhancing thermal conductivity. Moreover, compared with HEX-like and inverted HEX-like morphologies, which exhibited numerous thermal interfaces, the LAM-like morphology was able to construct long-range phonon transport pathways and reduce phonon scattering through the synergistic effect of microphase separation-driven confined assembly with a semicrystalline structure and supramolecular assembly, thereby exhibiting higher thermal conductivity. The λ of PLC11$_{50}$-*b*-PGMA$_{50}$ reached 0.27 W (m^{-1} K^{-1}), representing a 23% increase compared to 0.22 W (m^{-1} K^{-1}) for its random counterpart PLC11$_{50}$-*co*-PGMA$_{50}$ which displayed no multi-level long-range ordered structure. Further increasing the monomer ratio of LC11/GMA to 50/5 transformed its microstructure into the most regular and ordered morphology with the smallest interflake spacing (4.40 Å) that was dominated by the cyanobiphenyl units through supramolecular assembly, resulting in the highest λ of 0.29 W (m^{-1} K^{-1}) among the uncured copolymers. Importantly, this highly ordered structure of PLC11$_{50}$-*b*-PGMA$_5$ could be retained after curing, leading to the highest λ of 0.39 W (m^{-1} K^{-1}), which was 1.95 times that of traditional epoxy resin (E-51, 0.20 W (m^{-1} K^{-1})). In addition to the substantial fundamental interest, our findings demonstrate the critical role of long-range ordered structures in modulating the intrinsic thermal conductivity of polymers, serving as a new paradigm for the rational design of highly thermally conductive polymers for cutting-edge high-performance electronic systems.

Author contributions

Conceptualization: J. Z. Data curation, methodology, formal analysis, and writing – original draft: K. Z. and J. Z. Formal analysis: K. Z., J. Z., and J. A. Project administration, supervision, funding acquisition, and writing – review & editing: J. Z. and J. G.

Conflicts of interest

There are no conflicts to declare.

Data availability

The data supporting this article have been included as part of the supplementary information (SI). Supplementary information: materials, characterization methods, additional experimental details, supplementary figures and tables. See DOI: https://doi.org/10.1039/d6sc01804a.

Acknowledgements

The authors are grateful for the support from the National Natural Science Foundation of China (52473084, 52473083), Natural Science Basic Research Plan in Shaanxi Province of China (2024JC-YBMS-279), Natural Science Basic Research Program of Shaanxi (2024JC-TBZC-04), the Innovation Capability Support Program of Shaanxi (2024RS-CXTD-57), the Analytical & Testing Center of Northwestern Polytechnical University for SEM and TGA tests performed in this work.

Notes and references

1 X. Chen, K. Wu, Y. Zhang, D. Liu, R. Li and Q. Fu, *Adv. Mater.*, 2022, **34**, 2206088.
2 M. Xiao and B. X. Du, *High Volt.*, 2016, **1**, 34–42.
3 X. Zhong and J. Gu, *Trans. Mater. Res.*, 2026, **2**, 100184.
4 J. Li, X. Liu, Y. Feng and J. Yin, *Prog. Polym. Sci.*, 2022, **126**, 101505.
5 J.-W. Zha, F. Wang and B. Wan, *Prog. Mater. Sci.*, 2025, **148**, 101362.
6 X. Fan, Z. Liu, S. Wang and J. Gu, *SusMat*, 2023, **3**, 877–893.
7 G. Chen, Q. Zhang, Z. Hu, S. Wang, K. Wu, J. Shi, L. Liang and M. Lu, *J. Macromol. Sci., Part A:Pure Appl. Chem.*, 2019, **56**, 484–495.
8 Y. Liu, W. Zou, N. Zhao and J. Xu, *Nat. Commun.*, 2023, **14**, 5342.
9 G. Lv, B. Soman, N. Shan, C. M. Evans and D. G. Cahill, *ACS Macro Lett.*, 2021, **10**, 1088–1093.
10 J. Zhang, C. Tang, Q. Kong, M. He, P. Lv, H. Guo, Y. Guo, X. Shi and J. Gu, *Soft Sci.*, 2025, **5**, 9.
11 X. Wu, X. Zhang, X. Yan, C. Zhang, Y. Zhang, P. Li, N. Li, H. Liu and Z. Wang, *J. Polym. Sci.*, 2024, **62**, 2410–2442.
12 M. Dinpajooh and A. Nitzan, *J. Chem. Phys.*, 2020, **153**, 164903.
13 Z. Wang, Z. Wu, L. Weng, S. Ge, D. Jiang, M. Huang, D. M. Mulvihill, Q. Chen, Z. Guo, A. Jazzar, X. He, X. Zhang and B. B. Xu, *Adv. Funct. Mater.*, 2023, **33**, 2301549.
14 Y. Lin, P. Li, W. Liu, J. Chen, X. Liu, P. Jiang and X. Huang, *ACS Nano*, 2024, **18**, 3851–3870.
15 R. Roy, K. C. Stevens, K. A. Treaster, B. S. Sumerlin, A. J. H. McGaughey, J. A. Malen and A. M. Evans, *Mater. Horiz.*, 2024, **11**, 3267–3286.
16 K. Ruan, X. Shi, Y. Zhang, Y. Guo, X. Zhong and J. Gu, *Angew. Chem., Int. Ed.*, 2023, **62**, e202309010.
17 Q. Kong, J. Zhang, K. Zhang, S. Wang, M. He, Y. Guo and J. Gu, *Angew. Chem., Int. Ed.*, 2025, **64**, e202512721.
18 M. M. Hossain, A. I. Olamilekan, H.-O. Jeong, H. Lim, Y.-K. Kim, H. Cho, H. D. Jeong, M. A. Islam, M. Goh, N.-H. You, M. J. Kim, S. Q. Choi, J. R. Hahn, H. Yeo and S. G. Jang, *Macromolecules*, 2022, **55**, 4402–4410.
19 S. Wang, K. Ruan, Y. Guo, J. Kong and J. Gu, *Angew. Chem., Int. Ed.*, 2025, **64**, e202501459.
20 Y. Jia, Z. Mao, W. Huang and J. Zhang, *Mater. Chem. Phys.*, 2022, **287**, 126325.
21 H. Zhang, Y. Guo, Y. Zhao, Q. Zhu, M. He, H. Guo, X. Shi, K. Ruan, J. Kong and J. Gu, *Angew. Chem., Int. Ed.*, 2025, **64**, e202500173.
22 R. Shrestha, P. Li, B. Chatterjee, T. Zheng, X. Wu, Z. Liu, T. Luo, S. Choi, K. Hippalgaonkar, M. P. de Boer and S. Shen, *Nat. Commun.*, 2018, **9**, 1664.

23 X. Wei and T. Luo, *Phys. Chem. Chem. Phys.*, 2022, **24**, 10272–10279.
24 A. Shanker, C. Li, G.-H. Kim, D. Gidley, K. P. Pipe and J. Kim, *Sci. Adv.*, 2017, **3**, e1700342.
25 N. Jiang, Y.-Y. Song, L.-N. Wang, W.-W. Liu, L. Bai, J. Yang and W. Yang, *Adv. Funct. Mater.*, 2025, **35**, 2416277.
26 Y. Xu, D. Kraemer, B. Song, Z. Jiang, J. Zhou, J. Loomis, J. Wang, M. Li, H. Ghasemi, X. Huang, X. Li and G. Chen, *Nat. Commun.*, 2019, **10**, 1771.
27 K. Zhang, J. Zhang, L. Dang, Y. Wu, M. He, H. Guo, X. Shi, H. Qiu and J. Gu, *Sci. China: Chem.*, 2025, **68**, 2615–2627.
28 J. Zhang, L. Dang, F. Zhang, K. Zhang, Q. Kong and J. Gu, *JACS Au*, 2023, **3**, 3424–3435.
29 I. Jeong, C. Kim, D. Kang, K. Jeong, S. Jang, N. You, S. Ahn, D. Lee and M. Goh, *J. Polym. Sci., Part A: Polym. Chem.*, 2019, **57**, 708–715.
30 G. Lv, C. Shen, N. Shan, E. Jensen, X. Li, C. M. Evans and D. G. Cahill, *Proc. Natl. Acad. Sci. U. S. A.*, 2022, **119**, e2211151119.
31 K. Ku and H. Yeo, *Polym. Chem.*, 2023, **14**, 644–650.
32 K. Ku and H. Yeo, *ACS Appl. Polym. Mater.*, 2024, **6**, 13449–13456.
33 K. Ku and H. Yeo, *Ind. Eng. Chem. Res.*, 2024, **63**, 20059–20064.
34 H. Zhang, Z. Zhao, A. T. Turley, L. Wang, P. R. McGonigal, Y. Tu, Y. Li, Z. Wang, R. T. K. Kwok, J. W. Y. Lam and B. Z. Tang, *Adv. Mater.*, 2020, **32**, 2001457.
35 H. Tian, Y. Ma, Z. Li, M. Cheng, S. Ning, E. Han, M. Xu, P.-F. Zhang, K. Zhao, R. Li, Y. Zou, P. Liao, S. Yu, X. Li, J. Wang, S. Liu, Y. Li, X. Huang, Z. Yao, D. Ding, J. Guo, Y. Huang, J. Lu, Y. Han, Z. Wang, Z. G. Cheng, J. Liu, Z. Xu, K. Liu, P. Gao, Y. Jiang, L. Lin, X. Zhao, L. Wang, X. Bai, W. Fu, J.-Y. Wang, M. Li, T. Lei, Y. Zhang, Y. Hou, J. Pei, S. J. Pennycook, E. Wang, J. Chen, W. Zhou and L. Liu, *Nature*, 2023, **615**, 56–61.
36 X. Zhong, K. Ruan and J. Gu, *Sci. China: Chem.*, 2026, **69**, 1989–1996.
37 C. M. Bates and F. S. Bates, *Macromolecules*, 2017, **50**, 3–22.
38 Y. Kang, H. Wang, X. Li, F. Meng, H. Liu, Y. Xiao, Z. Jiang, H. Gao, C. Liu, F. Wang, L. Pan and Y. Li, *Macromolecules*, 2024, **57**, 4208–4219.
39 Z. Su, C.-H. Hsu, Z. Gong, X. Feng, J. Huang, R. Zhang, Y. Wang, J. Mao, C. Wesdemiotis, T. Li, S. Seifert, W. Zhang, T. Aida, M. Huang and S. Z. D. Cheng, *Nat. Chem.*, 2019, **11**, 899–905.
40 C. Lee and C. O. Osuji, *ACS Macro Lett.*, 2021, **10**, 945–957.
41 H. Takeshita, T. Shiomi, K. Takenaka and F. Arai, *Polymer*, 2013, **54**, 4776–4789.
42 Z. Tong, J. Zhou, R.-Y. Wang and J.-T. Xu, *Polymer*, 2017, **130**, 1–9.
43 L. Zhang, Z. Yang, W. Xia, J. Li, H. Yang, S. Yang and E.-Q. Chen, *J. Am. Chem. Soc.*, 2024, **146**, 31221–31229.
44 F. Cai, B. Yang, X. Lv, W. Feng and H. Yu, *Sci. Adv.*, 2022, **8**, eabo1626.
45 R. Li and Z. Shan, *Prog. Org. Coat.*, 2017, **104**, 271–279.
46 S. Weng, R. Zhao, X. Fu, J. Cai, K. Wang, Z. Lu and L. Hou, *ACS Macro Lett.*, 2025, **14**, 1579–1585.
47 F. Zhang, J. Zhang, K. Zhang, X. Zhong, M. He, H. Qiu and J. Gu, *Adv. Sci.*, 2025, **12**, 2410362.
48 S. Park, E. Nam, K. Ku and H. Yeo, *Eur. Polym. J.*, 2025, **239**, 114282.
49 S. Harrisson, *Polym. Chem.*, 2018, **9**, 1366–1370.
50 W. Chen, K. Wu, B. Nan and M. Lu, *React. Funct. Polym.*, 2019, **145**, 104370.
51 R. Wang and Z.-G. Wang, *Macromolecules*, 2010, **43**, 10096–10106.
52 W. Xu, C. Zhou, W. Ji, Y. Zhang, Z. Jiang, F. Bertram, Y. Shang, H. Zhang and C. Shen, *Angew. Chem., Int. Ed.*, 2024, **63**, e202319766.
53 T. Giang and J. Kim, *J. Electron. Mater.*, 2017, **46**, 627–636.
54 W. Wang, X. Wang, F. Jiang and Z. Wang, *Polym. Chem.*, 2018, **9**, 3067–3079.
55 M. Koga, K. Sato, S. Kang and M. Tokita, *Macromol. Chem. Phys.*, 2018, **219**, 1700332.
56 M. J. Rymaruk, C. T. O'Brien, C. György, B. Darmau, J. Jennings, O. O. Mykhaylyk and S. P. Armes, *Angew. Chem., Int. Ed.*, 2021, **60**, 12955–12963.
57 I. Hamley and V. Castelletto, in *Soft Matter Characterization*, ed. R. Borsali and R. Pecora, Springer Netherlands, Dordrecht, 2008, pp. 1021–1081.
58 Q. P. Chen, L. Barreda, L. E. Oquendo, M. A. Hillmyer, T. P. Lodge and J. I. Siepmann, *ACS Nano*, 2018, **12**, 4351–4361.
59 M. Li, P. Gong, Z. Zhang, L. Li, Y. Chen, Y. Qin, Y. Guo, R. Yang, J. Zhang, Y. Zhou, K. Xu, Y. Wang, H. Do, X. Jia, T. Cai, C.-T. Lin, N. Jiang and J. Yu, *Commun. Mater.*, 2024, **5**, 18.
60 S. Plimpton, *J. Comput. Phys.*, 1995, **117**, 1–19.
61 Y.-C. Yao and J.-X. Hou, *Pramana*, 2022, **96**, 36.